The wiggling trajectories of bacteria

Yunkyong Hyon, null Marcos, Thomas R. Powers, Roman Stocker and Henry C. Fu

The wiggling trajectories of bacteria

Yunkyong Hyon[1], **Marcos**[2], **Thomas R. Powers**[3], **Roman Stocker**[4]
and Henry C. Fu[1]†

[1] Department of Mechanical Engineering, University of Nevada, Reno, NV 89557, USA

[2] School of Mechanical and Aerospace Engineering, Nanyang Technological University,
Singapore 639798, Singapore

[3] School of Engineering and Department of Physics, Brown University, Providence, RI 02912, USA

[4] Ralph M. Parsons Laboratory, Department of Civil and Environmental Engineering,
Massachusetts Institute of Technology, Cambridge, MA 02139, USA

Many motile bacteria display wiggling trajectories, which correspond to helical swimming paths. Wiggling trajectories result from flagella pushing off-axis relative to the cell body and making the cell wobble. The spatial extent of wiggling trajectories is controlled by the swimming velocity and flagellar torque, which leads to rotation of the cell body. We employ the method of regularized stokeslets to investigate the wiggling trajectories produced by flagellar bundles, which can form at many locations and orientations relative to the cell body for peritrichously flagellated bacteria. Modelling the bundle as a rigid helix with fixed position and orientation relative to the cell body, we show that the wiggling trajectory depends on the position and orientation of the flagellar bundle relative to the cell body. We observe and quantify the helical wiggling trajectories of *Bacillus subtilis*, which show a wide range of trajectory pitches and radii, many with pitch larger than 4 μm. For this bacterium, we show that flagellar bundles with fixed orientation relative to the cell body are unlikely to produce wiggling trajectories with pitch larger than 4 μm. An estimate based on torque balance shows that this constraint on pitch is a result of the large torque exerted by the flagellar bundle. On the other hand, multiple rigid bundles with fixed orientation, similar to those recently observed experimentally, are able to produce wiggling trajectories with large pitches.

1. Introduction

In most descriptions of bacterial swimming, such as analyses of run-and-tumble behaviour or of swimming near boundaries, the trajectories of the bacteria are considered to be relatively straight, with radii of curvature much larger than the bacterial cell body, except for occasional sharp changes in direction (tumbles). However, it has long been observed that, when examined in detail, the cell bodies of bacteria 'wobble' (Berg & Brown 1972; Darnton *et al.* 2007), an indication that they

† Email address for correspondence: hfu@unr.edu

are constantly rotating. A consequence of this rotation is that the natural trajectory of bacteria is generally a helix (Keller & Rubinow 1976; Purcell 1977; Shapere & Wilczek 1989). Its two-dimensional projection, as typically visualized under a microscope, is a 'wiggling' trajectory.

Either because this fine-scale wiggling is difficult to resolve spatially and temporally, or because it is considered inconsequential for the net motion of the cell, wiggling has been ignored in both measurements and modelling of bacterial motility. Instead, the wiggle is averaged out and the cell's trajectory is considered to be the centreline of the actual helical trajectory. We shall refer to this averaged trajectory as the centreline trajectory.

Many aspects of bacterial motility can be adequately explained and modelled based purely on centreline trajectories. For example, during the run portions of run-and-tumble swimming, Berg & Brown (1972) measured the statistics of reorientation during a tumble of *Escherichia coli* by comparing the angle between the run portions of trajectories; their definition of run direction corresponds to centreline trajectories, not to wiggling trajectories. Accordingly, in models of run-and-tumble chemotaxis (e.g. Bearon & Pedley 2000; Locsei & Pedley 2009, and references therein) the transport of bacteria due to swimming corresponds to travel along centrelines. Since wiggling is deterministic, a random reorientation of the cell body due to Brownian rotational diffusion or tumbling results in a reorientation of equal magnitude of the centreline trajectory direction. However, there are cases when it is imperative to take into account the fine-scale wiggling. One example of this, helical klinotaxis, has been extensively discussed in the context of larger ($\approx$10 μm) organisms such as protists (Crenshaw 1996; Crenshaw, Ciampaglio & McHenry 2000). Helical trajectories may enhance the sensing of physicochemical stimuli, including chemical gradients and light.

Wiggling naturally arises from any arrangement of the flagellum or flagellar bundle that is not collinear with a symmetry axis of the cell body, or if the cell body or bundle is not symmetric. In general, wiggling can be influenced by time-varying orientations and deformations of the flagella during propulsion, as well as the detailed geometries of the bundle and the cell body. However, the most common models for bacterial propulsion typically consider polar flagella or flagellar bundles modelled as helices aligned with the axis of symmetry of a cell body, and hence cannot describe wiggling dynamics.

Here, we investigate the minimal model capable of producing wiggling dynamics, namely, a flagellar bundle modelled as a rigid helix with a fixed, non-symmetric position and orientation relative to a rotationally symmetric cell body. We investigate the dependence of wiggling trajectory parameters on the cell geometry and show that the actual trajectory depends on the position and orientation of the flagellum or flagellar bundle relative to the cell body. We compare our modelling results to observations of wiggling trajectories of *Bacillus subtilis*. This approach can complement the use of flagellar staining techniques to visualize flagellar bundles, especially since the latter often requires high-sensitivity detection systems. In § 2, we describe how a flagellar bundle pushing the cell off-axis leads to wiggling trajectories. In § 3, we develop the model used to calculate wiggling trajectories. Then in § 4 we examine the wiggling trajectories produced by a single flagellar bundle, and find that the pitch of the trajectory is limited to values below those often observed for *B. subtilis*. Finally, in § 5, we discuss how multiple flagellar bundles can produce wiggling trajectories with larger pitches.
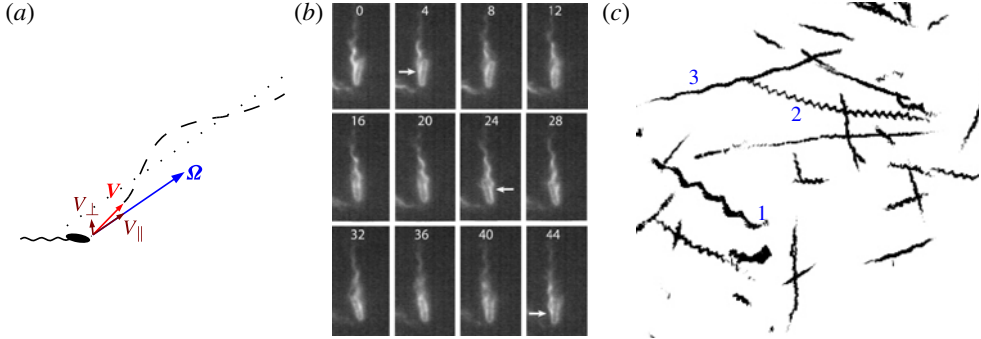
FIGURE 1. (Colour online) (*a*) A bacterium swimming with constant linear velocity V and angular velocity Ω in the body-fixed frame. Although in the body-fixed frame V and Ω are constant, in the space-fixed frame only Ω is constant and V rotates about Ω, leading to a helical trajectory around the direction of the rotation axis. The dashed line is the actual trajectory, while the dotted line is the centreline trajectory that one obtains if the wiggling is averaged out. (*b*) Frames from a video of an *E. coli* bacterium show that the cell body wobbles during swimming. Labels correspond to frame numbers, with frames spaced by 2 ms. Reproduced from Darnton *et al.* (2007), with permission from the American Society for Microbiology. (*c*) Trajectories of *B. subtilis* show different degrees of wiggling. Trajectories were obtained from frames acquired at 8.2 ms intervals with a 1600×1200 pixel charge-coupled device camera mounted on an inverted microscope equipped with a $40\times$ objective. This smooth-swimming strain, *B. subtilis* OI4139 (Szurmant, Muff & Ordal 2004), was grown in Cap assay minimal medium (Zimmer *et al.* 2002) and swam at a mean speed of 50 μm s^{-1}. The trajectories labelled 1, 2 and 3 have pitch and radius of: (i) 7.3 μm and 1.1 μm; (ii) 3.0 μm and 0.6 μm; and (iii) 10.3 μm and 0.4 μm.

2. The kinematics of wiggling

A helical trajectory is the general result of a swimmer undergoing a periodic swimming stroke in a body-fixed reference frame (Keller & Rubinow 1976; Purcell 1977; Shapere & Wilczek 1989). Over one stroke, the swimmer will both rotate and translate, arriving at a new position and orientation at the end of the stroke. During the next stroke, the swimmer rotates and translates by the same amounts relative to the body-fixed axes, which are now rotated with respect to the original frame. The net result of many swimming strokes is a helical trajectory.

It is simplest to understand the kinematics of such a trajectory by considering bacteria that swim using a single polar flagellum (monotrichous bacteria) or a single bundle of flagella (peritrichous bacteria) with a fixed orientation relative to the cell body. In the body-fixed frame, one may describe the motion induced by the rotation of the flagellum or flagellar bundle as a constant counter-rotation of the cell body combined with a constant translation of the entire cell (figure 1*a*). To analyse the resulting helical trajectory, the axis of rotation in a space-fixed frame remains constant, so that the rotation axis Ω (figure 1*a*) must coincide with the axis of the helical trajectory. The distance travelled in the direction of the axis of rotation during one flagellar revolution thus determines the pitch,

$$P = TV_{\parallel}, \tag{2.1}$$

where T is the period of one flagellar revolution, $V_{\parallel} = V \cdot \Omega/|\Omega|$ is the component of the swimming velocity along the rotation axis, and V and Ω are the instantaneous translational and angular velocities of the cell body, respectively. The radius of the
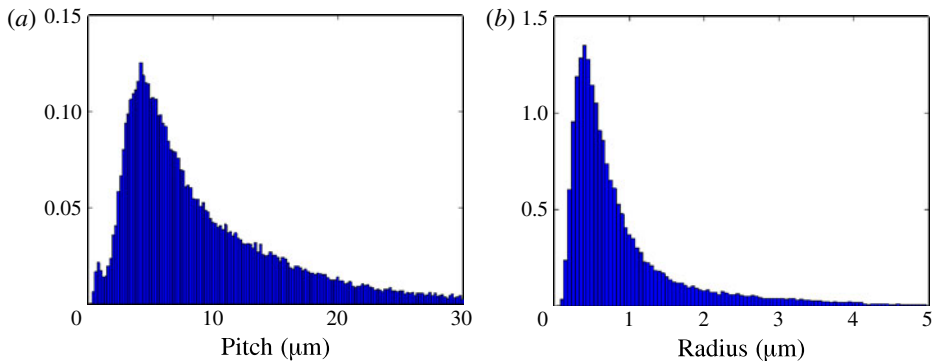
FIGURE 2. (Colour online) Probability distribution functions of (*a*) pitch and (*b*) radius of observed wiggling trajectories of *B. subtilis* OI4139. The mean pitch and radius were 8.9 ± 6.0 μm and 0.91 ± 0.81 μm, respectively (6.9 and 0.62 μm median pitch and radius, respectively). Images were analysed using BacTrack, an in-house cell-tracking Java software. BacTrack locates bacteria in each image and tracks them between two consecutive images, by applying a search radius (the maximum distance a bacterium can move between successive images). We applied a linear least-squares fit to each trajectory to obtain the centreline trajectory. The trajectory radius was determined from the root mean square (r.m.s.) of the perpendicular distance from each data point to the centreline. The trajectory pitch was determined as twice the average distance between consecutive crossings of the centreline. Trajectories with pitch greater than 30 μm or radius greater than 5 μm were discarded because upon visual inspection they did not correspond to wiggling trajectories. Pitches and radii from 72 087 trajectories are included in the data shown.

helical trajectory, R, is then obtained by noting that during one period, T, the velocity perpendicular to the rotation axis takes the swimmer around a circle of circumference $2\pi R$. Thus,

$$R = TV_\perp/(2\pi), \tag{2.2}$$

where $V_\perp = |V \cdot (I - \Omega\Omega/|\Omega|^2)|$ is the velocity component perpendicular to the rotation axis. Hence, specifying the wiggling trajectory's pitch, radius, and instantaneous swimming speed is equivalent to specifying the instantaneous translational and angular velocities of the cell body. We note that when V and Ω become parallel, the radius becomes zero and the trajectory is straight. For these straight trajectories, the pitch in a geometric sense is ill-defined because the trajectory repeats after any length travelled, but the pitch as defined by (2.1) remains well-defined and is the limit of the pitch obtained as V and Ω continuously approach coincident directions.

   The precise wiggling kinematics varies among different species of bacteria and even among individuals within a species. For example, Darnton *et al.* (2007) reported that *E. coli* swim with the long axis of their cell bodies making an average angle of 23° with the centreline trajectory (figure 1*b*). They observed the cell body rotating around the average trajectory direction, but the radius of the helical trajectory was too small to be directly observed. Different wiggling kinematics are observed for *B. subtilis*. We have imaged the trajectories of a smooth-swimming (i.e. non-tumbling) strain of *B. subtilis* and processed the images to track the position of the centre of cell bodies. Representative recordings (figure 1*c*) reveal that *B. subtilis* exhibits wiggling trajectories. Figure 2 shows the probability distribution functions of pitch and

radius for observed wiggling trajectories. The average pitch and radius were 8.9 and 0.91 μm, respectively, although it should be kept in mind that the pixel dimension was 0.38 μm. Additionally, substantial variability among trajectories is evident; the standard deviations for the pitch and radius were 6.0 and 0.81 μm, respectively. In figure 1(*c*) we have labelled three trajectories with radii varying from 0.4 to 1.1 μm and pitches varying from 3.0 to 10.3 μm, and listed their pitches and radii in the caption.

Since the flagellar bundle in peritrichously flagellated species like *E. coli* and *B. subtilis* can form at many positions and can be oriented in many possible directions, we focus on how altering flagellar bundle configuration affects wiggling bacterial trajectories.

3. Off-axis flagellar configurations produce wiggling

First consider a flagellar bundle located at the pole of a symmetric cell body and oriented collinearly with the major axis of the cell body. Owing to the symmetry there will be nearly no wiggling. In principle, the symmetry is broken by the phase angle of the rotating bundle, which leads to slight helical deviations from a straight path (Keller & Rubinow 1976); however, the flagellar rotation is much faster than the counter-rotation of the cell body, so that this symmetry breaking is averaged out over time scales much shorter than those relevant for the cell-body dynamics we describe here. Therefore, over time scales longer than a flagellar rotation period, the cell body merely counter-rotates against the flagellar rotation. In other words, the angular and translational velocities of the cell body are parallel, leading to nearly straight trajectories.

The wiggling we are concerned with therefore occurs when a flagellar bundle is attached to the cell body in an off-axis configuration. In this case, the flagellar thrust produces a torque on the cell body that leads to cell-body rotation beyond the usual counter-rotation produced at the rotary flagellar motor. The net result is that the overall angular velocity of the cell body is no longer parallel to the translational velocity of the cell body, generating a wiggling helical trajectory.

3.1. *Boundary element method*

To investigate the dependence of the shape of the helical trajectory on the flagellar configuration, we calculate trajectories for a range of configurations using the method of regularized stokeslets (Cortez 2001; Cortez, Fauci & Medovikov 2005), a type of boundary element method (BEM). Boundary element methods (Goto *et al.* 1910; Phan-Thien, Tran-Cong & Ramia 1987; Ramia, Tullock & Phan-Thien 1993; Flores *et al.* 2005; Smith *et al.* 2009; Shum, Gaffney & Smith 2010) have been used extensively to model swimming bacteria. In the method of regularized stokeslets, the flow is modelled as due to localized forces at the surface of the cell body and flagellum. In contrast to the stokeslet, which is the flow field caused by a point force acting on the fluid, the regularized stokeslet is the flow field established by a smooth, localized distribution of force (Cortez 2001). The total velocity field is

$$v_i(\boldsymbol{r}) = \sum_{\alpha}^{N} S_{ij}(\boldsymbol{r} - \boldsymbol{r}_\alpha) f_j^\alpha, \tag{3.1}$$

where $\boldsymbol{r}_\alpha$ is the location of the localized force $\boldsymbol{f}^\alpha$, and $S_{ij}(\boldsymbol{r}) = [(r^2 + 2\epsilon^2)\delta_{ij} + r_i r_j]/[8\pi\mu (r^2 + \epsilon^2)^{3/2}]$ is the regularized stokeslet. The parameter ϵ represents the

width of an individual stokeslet's force distribution, which takes the form $15\boldsymbol{f}^{\alpha}\epsilon^4/[8\pi\,(r^2+\epsilon^2)^{7/2}]$ for a net force $\boldsymbol{f}^{\alpha}$ centred at the origin.

To specify the flow we must determine the forces $\boldsymbol{f}^{\alpha}$, which in turn are determined if we know the velocity field at N points, since (3.1) is an invertible linear system of equations. Equation (3.1) is evaluated to provide the velocity at each of the N positions $\boldsymbol{r}_{\alpha}$ on the surface of the swimmer. The regularization of the stokeslet prevents singularities of the flow field at the positions $\boldsymbol{r}_{\alpha}$. The velocities at the surface points can in turn be determined from no-slip boundary conditions and the swimming velocity, cell-body angular velocity and the prescribed swimming stroke:

$$\boldsymbol{v}(\boldsymbol{r}_{\alpha}) = \boldsymbol{V} + \boldsymbol{\Omega} \times \boldsymbol{r}'_{\alpha} + \delta\dot{\boldsymbol{r}}_{\alpha}, \qquad (3.2)$$

where $\boldsymbol{r}'_{\alpha}$ are the positions measured from the centroid of the cell body. The swimming stroke is specified by $\delta\dot{\boldsymbol{r}}_{\alpha}$, which is the velocity of surface elements relative to the centroid of the cell body in a body-fixed frame; in our case they specify that the flagella rotate relative to the cell body at a fixed angular frequency. This reduces the problem to six unknown degrees of freedom, the components of $\boldsymbol{V}$ and $\boldsymbol{\Omega}$, which are solved for by applying the conditions of zero total force and zero total torque appropriate for a freely suspended swimmer,

$$0 = \sum_{\alpha} \boldsymbol{f}^{\alpha}, \qquad (3.3)$$

$$0 = \sum_{\alpha} \boldsymbol{r}'_{\alpha} \times \boldsymbol{f}^{\alpha}. \qquad (3.4)$$

From the resulting linear system of equations, we determine the instantaneous swimming velocity and the angular rotation of the cell body as a function of the geometry of the swimmer and the swimming stroke, which is specified by the rotation rate of the flagellar bundle relative to the cell body.

3.2. *Bacterial geometry and discretization*

The cell body is modelled as an ellipsoid. The surface of the ellipsoid is discretized using a mesh generation scheme for implicit geometries due to Persson (2005). At each node of the discretization, we place one regularized stokeslet. The average separation between neighbouring stokeslets on the surface of the cell body is denoted by Δs_c.

In peritrichous bacteria, a flagellar bundle is composed of multiple flagella that come together to rotate synchronously. The hook at the base of a flagellum provides the compliance necessary to allow the formation of a bundle from multiple flagella attached at different locations. Owing to this compliance, the bundle may be able to vary its position and orientation relative to the cell body during propulsion. The bundle is a composite of many flagellar helices so its shape may not be precisely helical, especially at the base where flagella from different locations enter the bundle. Nonetheless, since studies of bundle dynamics (Flores *et al.* 2005; Janssen 2011) and geometries do not currently provide detailed guidance for bundle geometry and dynamics, we use a minimal model capable of producing wiggling trajectories that treats the flagellar bundle as a rigid helix with a fixed position and orientation (apart from rotation about the helical axis) relative to the cell body. Away from the hook, flagella are stiffer, and modelling them as rigid helices can be justified by the experiments by Magariyama *et al.* (2005). These experiments verified the calculation

of Takano *et al.* (2003), who found that for an individual flagellum flows generated by swimming deform the flagellum by less than 3 %.

To prevent the close approach of the flagella and cell body, especially when the bundle is off-axis, we taper the bundle's helical radius near the cell body. When the bundle lies along the *x*-axis, the centreline of the bundle filament is given by

$$\boldsymbol{r}(s) = -s\hat{\boldsymbol{x}} + [1 - \mathrm{e}^{-s^2/k_E^2}]r[\cos(2\pi s/p)\hat{\boldsymbol{y}} + \sin(2\pi s/p)\hat{\boldsymbol{z}}], \tag{3.5}$$

where p and r are the pitch and radius of the flagellar bundle, s is the distance along the axis of the helix, ranging from 0 to the length of the helix L, and k_E is the characteristic length of the tapering region. This flagellum geometry has previously been used extensively in the literature (Phan-Thien *et al.* 1987; Ramia *et al.* 1993; Shum *et al.* 2010).

The surface of the flagellar bundle is discretized as follows. The bundle is cut into cross-sections that are normal to the centreline of the helix. Regularized stokeslets are placed at n equally spaced points around this cross-section, i.e. at the vertices of a regular n-gon. At the next cross-section, another n-gon is constructed, but rotated so that each regularized stokeslet has two nearest neighbours in the n-gon of the previous cross-section. An integer number of evenly spaced cross-sections are chosen such that the spacing of nearest-neighbour stokeslets between adjacent cross-sections is as close as possible to the distance between the vertices of the n-gon. We denote the mean spacing between nearest neighbour stokeslets on the tail with Δs_f. The first and last cross-sections lie at the faces of the flagellar filament, specified by $s = 0$ and $s = L$. Finally, hemispherical caps are placed at the ends of the flagellar filament. The caps are discretized using the grid method described in Cortez *et al.* (2005); the spacing between elements on the equator is chosen to be as close as possible to Δs_f.

3.3. *Validation of boundary element method*

3.3.1. *Ellipsoids*

We first validate the BEM by calculating the translational and rotational resistance coefficients of an ellipsoid, and comparing them to analytical results (Steinberger *et al.* 1994). To calculate the translational (rotational) velocity due to an external force (torque), the equation for force (torque) balance, equation (3.3) (equation (3.4)) is modified to include a net external force (torque) on the left-hand side.

Analytic results (Happel & Brenner 1965) indicate that for a prolate ellipsoid moving through a fluid in the Stokes limit, the total force $\boldsymbol{F}$ and total torque $\boldsymbol{N}$ are linearly related to the translational and rotational velocities $\boldsymbol{V}$ and $\boldsymbol{\Omega}$, respectively, and are given by $\boldsymbol{F} = C_{T1}\boldsymbol{V}$ and $\boldsymbol{N} = C_{R1}\boldsymbol{\Omega}$, for $\boldsymbol{V}$ and $\boldsymbol{\Omega}$ parallel to the major axis; and by $\boldsymbol{F} = C_{T2}\boldsymbol{V}$ and $\boldsymbol{N} = C_{R2}\boldsymbol{\Omega}$, for $\boldsymbol{V}$ and $\boldsymbol{\Omega}$ in the plane of the minor axes. For the cell-body ellipsoid with major semi-axis $4b$ and minor semi-axis b moving through a fluid with dynamic viscosity μ, the analytic results give $C_{T1}^A = 30.1\mu b$, $C_{T2}^A = 38.3\mu b$, $C_{R1}^A = 72.5\mu b^3$ and $C_{R2}^A = 341\mu b^3$ (Steinberger *et al.* 1994). In figure 3 we plot the values of the four resistance coefficients normalized by the analytic results as a function of the number of regularized stokeslets. The different curves correspond to different values of stokeslet regularization parameter to stokeslet spacing ($\epsilon/\Delta s$). The numerical values converge on the analytic results. For the ellipsoid, the fastest convergence is obtained for $\epsilon/\Delta s = 1/3$, for which the average error is 0.99 % using 1712 stokeslets (which is the number we use to discretize the bacterial cell body). For $\epsilon/\Delta s = 1$, the average error is 5.2 % using 1712 stokeslets.
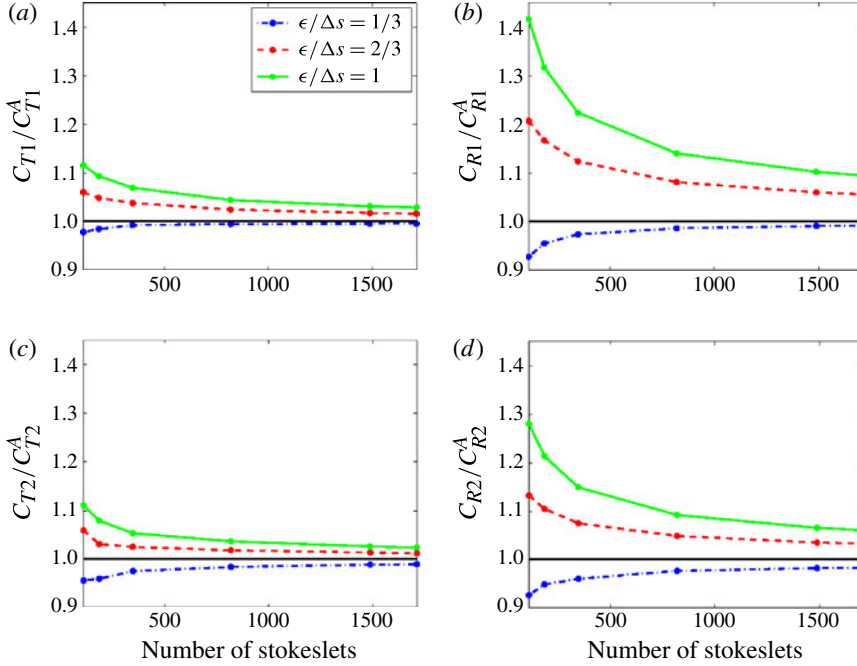
FIGURE 3. (Colour online) Validation of BEM by calculation of the resistance coefficients for an ellipsoid: (a) C_{T1}, (b) C_{R1}, (c) C_{T2} and (d) C_{R2}, all normalized by their analytic values C_{T1}^A, C_{R1}^A, C_{T2}^A and C_{R2}^A, respectively, as a function of number of stokeslets used to discretize the ellipsoid surface.

3.3.2. *Bacterial geometries*

We validate our calculations of bacterial swimming velocities by comparing results to the BEM calculations reported by Phan-Thien *et al.* (1987). Those authors used the same form of flagellar centreline as in (3.5) and reported swimming speeds for spherical cell bodies and a variety of flagellar geometries, calculated using a BEM. They compared their results to those calculated using the slender-body theory of Higdon (1979). We calculate the swimming speed for the same flagellar geometries but with our own discretization scheme, with cross-sections represented by 18-gons, and 1608 regularized stokeslets discretizing the cell body. These choices lead to a stokeslet separation on the cell body (Δs_c) that is approximately 23.5 times as large as the stokeslet separation on the bundle (Δs_f). The regularization parameter ϵ is chosen to be equal to Δs_c on the cell body and to Δs_f on the flagellar bundle (as justified in § 3.4).

Representative results are shown in figure 4. There, the cell body has radius a, the contour length of the flagellar filament is $5a$, and the radius of the filament centreline is $r = 2\pi/p$, where p is the pitch. In figure 4(a) the swimming speed is plotted as a function of the number of turns of the helical flagellar filament, N_λ, and the radius of the flagellar filament, r_f, is held constant at $r_f = 0.02a$. The pitch, p, of the filament centreline varies inversely with the number of turns N_λ. In figure 4(b) the swimming speed is plotted as a function of the radius of the flagellar filament r_f, and the number of turns is held constant at $N_\lambda = 1$, hence the pitch is also constant. Figure 4 shows that there is good agreement between our BEM, Phan-Thien *et al.* (1987) and
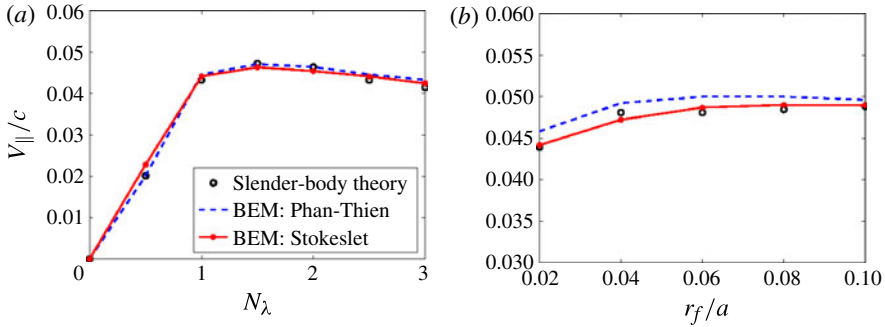
FIGURE 4. (Colour online) Validation of the BEM by comparison to the BEM results of Phan-Thien *et al.* (1987) and the slender-body theory of Higdon (1979). (*a*) Component of swimming velocity in the rotation direction ($V_\parallel$) normalized by helical wave speed *c* as a function of the number of turns N_λ, as in figure 2 of Phan-Thien *et al.* (1987). (*b*) Plot of $V_\parallel/c$ as a function of the ratio of the flagellum filament radius to cell-body radius (r_f/a), as in figure 5 of Phan-Thien *et al.* (1987).

slender-body theory. Across figure 4, the average discrepancy is 2.6 % relative to the results of Phan-Thien *et al.* and 3.2 % relative to the slender-body theory. In figure 4(*a*) the maximum discrepancy is 13.5 % for half a turn ($N_\lambda = 0.5$), but for three turns (the number of turns in our *B. subtilis* model) the discrepancy is 1.9 % relative to Phan-Tien *et al.* and 2.3 % relative to slender-body theory. In figure 4(*b*) the maximum discrepancy is 1.8 % relative to Phan-Thien *et al.* and 4.1 % relative to slender-body theory.

3.4. *Geometry for Bacillus subtilis*

We model the bacterial cell body as an ellipsoid with major and minor axes of 4 and 1 μm, respectively, corresponding to the typical size of the cell body of *B. subtilis* in our experiments. In reality *B. subtilis* often have pill-shaped cell bodies which may not be completely symmetric; we discuss the possible effects of more realistic body shapes in § 6.

The flagellar bundle is modelled as a three-turn helix with a pitch angle of 37° and a length along the helical axis of 6 μm, according to values measured in the literature (Fujii, Shibata & Aizawa 2008). The bundle contains approximately 7–8 individual flagella, each of diameter approximately 12–20 nm (Li 2010). The packing fraction within the bundle is not known, so we pick a bundle filament radius of 45 nm. (For a close-packed bundle of 20 nm thick flagella, the bundle filament radius would be 30 nm; we discuss the effect of varying the bundle filament radius in § 6.) We prescribe the rotation rate of the flagellar bundle about its helical axis to be 150 rotations per second relative to the cell body, which yields a swimming velocity of 17.9 μm s^{-1} in the polar, on-axis configuration. These are physically reasonable values based upon our observed speeds of *B. subtilis*. More importantly, our results for trajectory shapes are not sensitive to the precise rotation rate (or swimming speed, which varies proportionally to rotation rate), since the shape of the helical trajectory depends only on the ratio of the swimming velocity and the flagellar rotation rate.

In contrast to the geometry used in Phan-Thien *et al.* (1987), the flagellum is not directly attached to the body. Instead, as in Ramia *et al.* (1993) and Shum *et al.* (2010), the flagellum base is separated from the cell body by a gap to prevent the
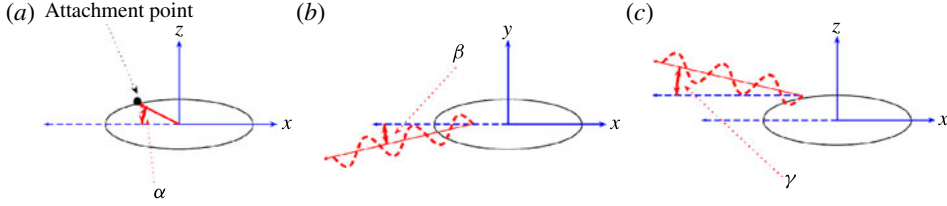
FIGURE 5. (Colour online) Schematic illustrating the definitions of the angle (*a*) α of the attachment point between the flagellar bundle and the ellipsoidal body, and the angles (*b*) β and (*c*) γ specifying the orientation of the flagellar bundle.

close approach of moving surfaces. Accurate treatment of two nearby moving surfaces requires that the separation between the surfaces be larger than the spacing between regularized stokeslets, Δs (Ramia *et al.* 1993). Since (as detailed later in this section) the stokeslet spacing in the cell body is $\Delta s_c = 0.07$, we choose a gap of 0.3625 µm, approximately five times as large as the stokeslet spacing.

The flagellar configuration can be specified using three angles (figure 5): one for the attachment point, and two for the orientation of the flagellum. Relative to a body-fixed coordinate system $\{\hat{e}_1, \hat{e}_2, \hat{e}_3\}$, where $\hat{e}_1$ is aligned with the major axis of the cell body, the angle α from the $-x$-axis specifies the attachment point, while the angles β and γ specify the orientation of the flagellum. Note that values of β that correspond to mirror-image bundle configurations (e.g. $\beta = 37°$ and $\beta = 360°-37° = 323°$) are distinct and do not yield the same wiggling trajectories, because the chirality of the helical flagellum breaks the mirror symmetry.

In figure 6 we plot the calculated translational and angular velocities V and Ω of the cell body as a function of the number of stokeslets per flagellum cross-section (n) for a representative flagellar configuration geometry, demonstrating the convergence of our results as the discretization becomes finer. The different curves correspond to different values of the ratio of stokeslet regularization parameter ϵ to stokeslet separation $\Delta s_{c,f}$. In contrast to the ellipsoidal geometry, for the bacterial geometry $\epsilon/\Delta s = 1$ led to the fastest convergence; hence we only calculated the computationally intensive case of $n = 24$ for $\epsilon/\Delta s = 1$, and use this value for the remainder of our calculations.

For $\epsilon/\Delta s = 1$, the values of $|V| = 16.29$ µm s^{-1} and $|\Omega| = 34.68$ rad s^{-1} for $n = 12$ are within 3.5 % of the results for $n = 24$ ($|V| = 16.88$ µm s^{-1} and $|\Omega| = 35.74$ rad s^{-1}); while the values of $P = 2.88$ µm and $R = 0.102$ µm are within 0.6 % of the results for $n = 24$ ($P = 2.90$ µm and $R = 0.102$ µm). Therefore, in order to reduce computational time, the calculations in §4 use $n = 12$, for which $\Delta s_f = 0.007\,85$ and the total number of regularized stokeslet in the discretization of the flagellar bundle is 4204. The discretization of the cell body uses 1712 regularized stokeslets, leading to $\Delta s_c = 0.07$. In figure 7 we show the resulting discretization for one flagellar configuration.

In order to compute the helical wiggling trajectory, it is important to realize that even in the body frame, the translational and rotational velocities are not constant, because the geometry of the bacterium changes as a result of the rotation of the flagellar bundle. We calculate the instantaneous translational and angular velocities of the cell body at time intervals corresponding to 1/32nd of a flagellar rotation period. We then integrate the velocities to find the net displacement and rotation of the cell body after a complete flagellar rotation. The average translational and angular
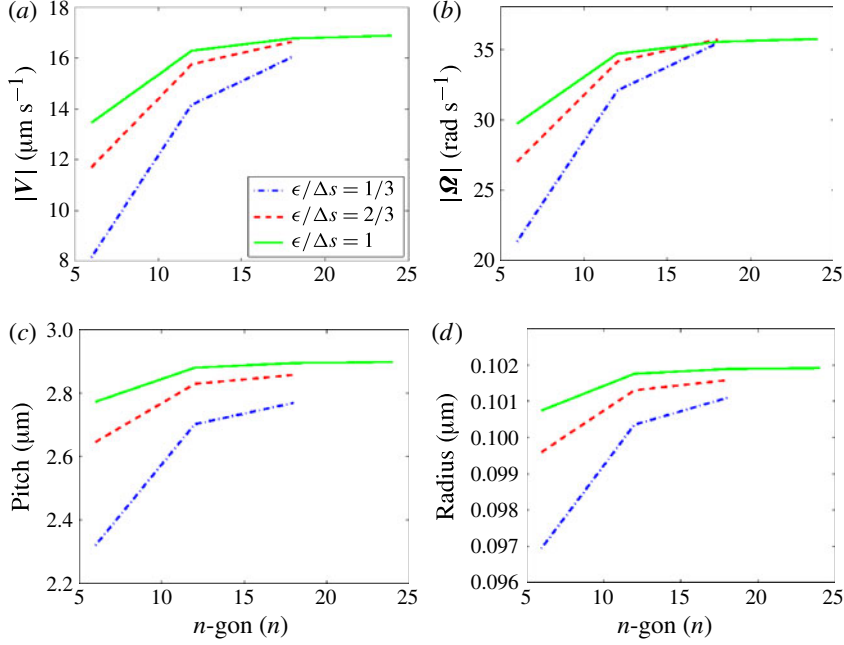
FIGURE 6. (Colour online) The kinematic parameters (*a*) swimming speed $|V|$, (*b*) cell-body rotation rate $|\Omega|$, (*c*) helical trajectory pitch P and (*d*) radius R, as functions of n, the number of stokeslets used to discretize a cross-section of the flagellar bundle. The different curves correspond to different values of the ratio of stokeslet regularization parameter ϵ and stokeslet separation Δs. Results are for the flagellar configuration specified by $\alpha = 74°$, $\beta = 323°$ and $\gamma = 61°$.
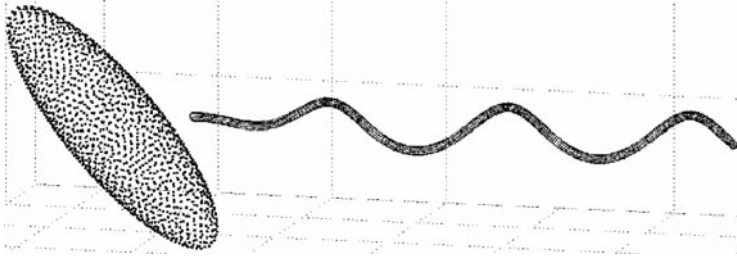

FIGURE 7. The model bacterium has a 1×4 µm ellipsoidal body. Each point on the surface of the bacterium corresponds to the location of a regularized stokeslet. There are 1712 stokeslets on the cell body and 4204 stokeslets on the flagellar bundle. Shown here is the configuration with flagellar angles $\alpha = 74°$, $\beta = 323°$ and $\gamma = 62°$.

velocities are calculated by dividing the net displacement and rotation by the flagellar rotation period. The pitch and radius of the helical trajectory are calculated using these average velocities in (2.1) and (2.2).

While one should in principle construct the helical trajectory by discrete iterations of the translation and rotation produced by one flagellar rotation, the error induced by instead using average velocities (equations (2.1) and (2.2)) is minimal, because there are $\geqslant 10$ flagellar rotations for each period of the helical trajectory. For the flagellar

configuration in figure 6, we verified that the translational and rotational velocities are only slightly changed by decreasing the time step from 1/32nd to 1/64th of the flagellar rotation period; decreasing the time step in this fashion changed the pitch and radius of the trajectory by 0.0038 and 0.077 %, respectively.

Note that different results are obtained by calculating the average translational and angular velocities by a simple average of the body-frame velocities over the 32 flagellar positions. This simple average leads to large errors in the radius and pitch, because the body frame constantly changes during one rotation of the bundle owing to flagellar propulsion. This type of error is less important for on-axis geometries without wiggling (Ramia *et al.* 1993; Shum *et al.* 2010).

4. Wiggling trajectories of *Bacillus subtilis* with one flagellar bundle

We calculated the trajectories produced by the entire range of flagellar bundle configuration geometries by varying the angles α, β and γ. Figure 8(*a–h*) shows the pitch (P) or radius (R) as a function of flagellar orientation angles β and γ for a fixed value of α. The range from $\alpha = 0°$ (polar bundle) to $\alpha = 90°$ encompasses all possible flagellar configuration geometries. We varied the angles α, β and γ in 15° increments, but figure 8 only shows the results for selected α. We excluded unphysical parameters for which the flagellum and cell body overlap.

The pitch and radius both vary from roughly 0 to 4 μm. There is the least variation in pitch as a function of configuration angle when $\gamma \approx 90°$ or $\beta \approx \pm 90°$; otherwise there can be quite strong variations in pitch as the angles β and γ vary. A notable feature of these results is that through the entire range of flagellar configurations the pitch is never greater than 4 μm (precisely, 3.875 μm). Since 81.5 % of the observed wiggling trajectories of *B. subtilis* in figure 2 have pitches greater than 3.875 μm, this result provides strong evidence that a single flagellar bundle cannot explain all of the observed swimming kinematics of *B. subtilis*.

In figure 9 we compare the pitch and radius obtained for each of our calculated trajectories to those of our experimentally observed trajectories; the calculated trajectories occupy a markedly smaller space in pitch–radius space than the observed trajectories. While the range of radius in our calculated trajectories is comparable to the range in our calculated trajectories, it is clear that many of the observed trajectories have pitch larger than those generated by our model.

4.1. *Physical constraint on maximum pitch from a single flagellar bundle*

To understand why a single flagellar bundle cannot produce wiggling trajectories with large pitch, we return to the kinematics described in §2. The pitch is the distance travelled in the direction of $\boldsymbol{\Omega}$ by the cell body during one period of body rotation ($T = 2\pi/|\boldsymbol{\Omega}|$). Thus, an upper bound on the pitch can be obtained as $2\pi V_{max}/\Omega_{min}$, where V_{max} is the maximum swimming speed and Ω_{min} is the minimum rotation rate. Among the trajectories for flagellar bundle configurations calculated in §4, $V_{max} \approx 22$ μm s^{-1} and $\Omega_{min} \approx 25$ s^{-1}, leading to an estimated maximum pitch of approximately 5.5 μm.

A physical constraint on the maximum pitch is set by the smallest cell-body rotation rate Ω_{min}. In turn, the minimum counter-rotation rate is determined from the torque produced by rotation of the flagellar bundle (from our BEM calculations, 1.54 pN μm for a bundle rotating at 150 Hz) and the maximum rotational resistance coefficient of the cell body, C_{Rmax}. This C_{Rmax} can be estimated as the resistance coefficient for the cell body rotating about an axis parallel to a minor axis and intersecting the polar end
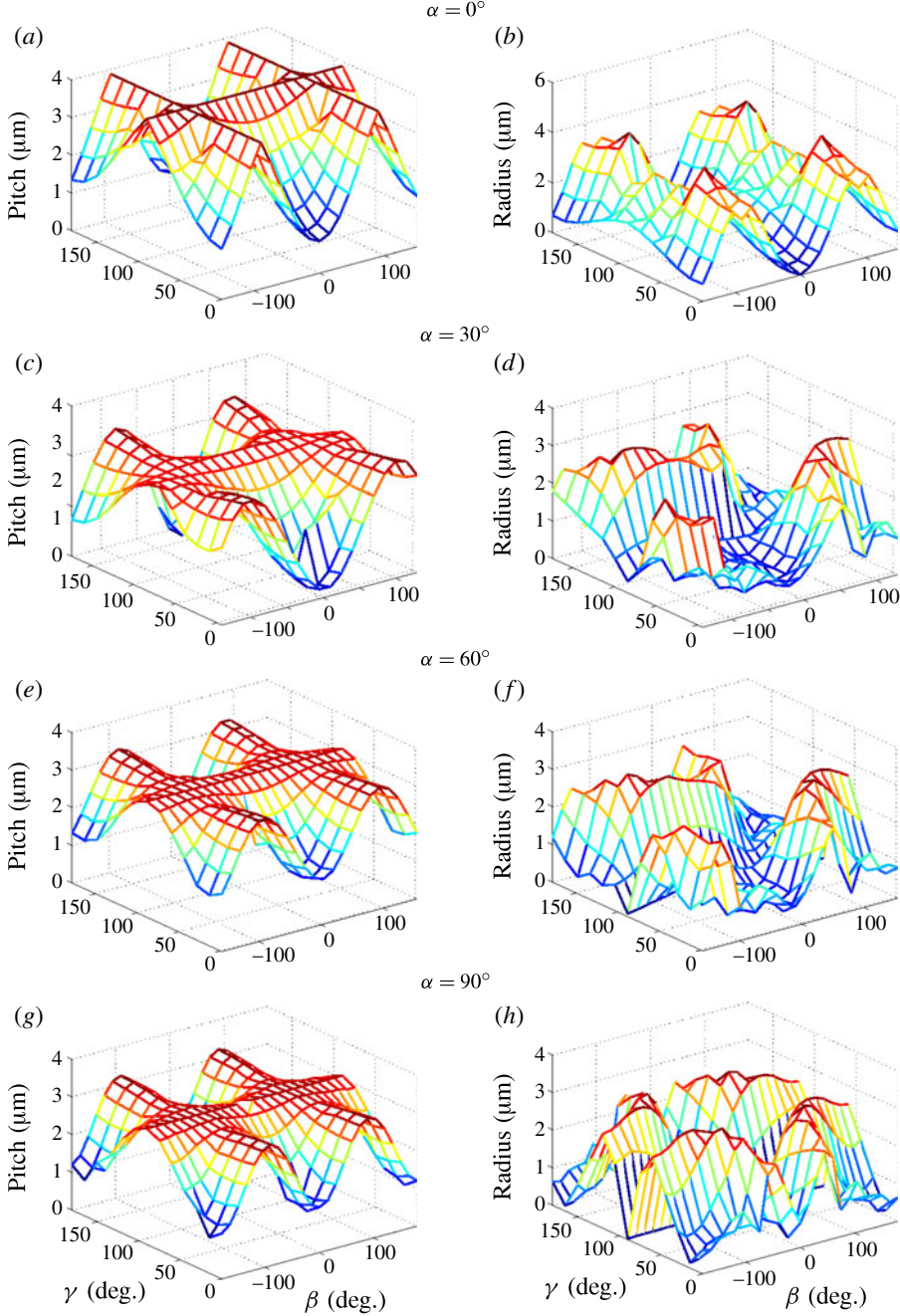
FIGURE 8. (Colour online) The pitch P and radius R of trajectories of *B. subtilis* calculated using our BEM. By varying the flagellar configuration angles (see figure 5), we explore the entire parameter space of possible flagellar configurations. The angle specifying the attachment point (α) takes a fixed value, while the angles specifying the orientation of the bundle (β and γ) vary.
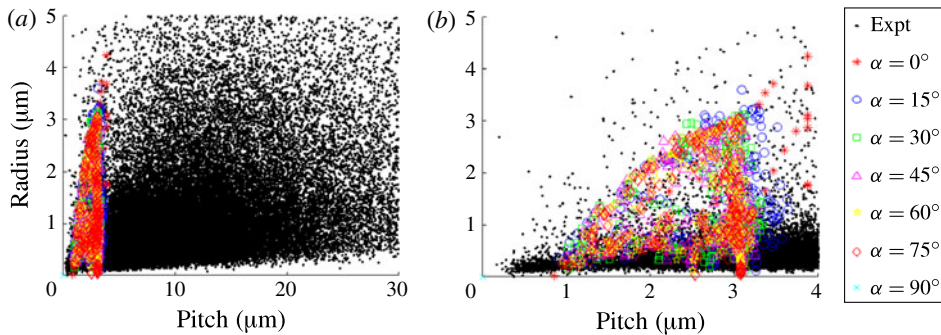
FIGURE 9. (Colour online) Scatter plots of pitch P and radius R of trajectories calculated using our BEM for *B. subtilis* with a single flagellar bundle (colour symbols), and of trajectories observed in our experiments (black points, obtained as in figure 2). Panel (*b*) shows a magnified view of the small-pitch region of panel (*a*).

of the cell body, $C_{R2} + C_{T2}(4b)^2 = 0.12$ pN µm s. Together, the torque and resistance coefficient lead to an upper bound for the pitch generated by a single flagellum of 10.7 µm. This upper bound is somewhat larger than the maximum pitch of 4 µm calculated with the BEM, but our estimate is rather conservative; in particular V_{max} leads to a significant overestimate because the relevant velocity is the component of velocity in the direction of Ω, not the entire swimming speed. Furthermore, when the flagellum is in the configuration producing C_{Rmax}, the swimming speed is slower because of additional drag from the cell body.

Nonetheless, this analysis sheds light on the physical reason why a single flagellar bundle cannot produce a large pitch: the flagellar torque required for propulsion is too large, and induces counter-rotation rates of the cell body that are too fast to allow the bacterium to travel very far during one rotation of the cell body. Thus, generically, wiggling trajectories of bacteria result from a flagellum or flagellar bundle pushing the cell body off-axis, while the period of the wiggle (hence, wiggle dimension) is limited by the swimming speed and flagellar torque.

This analysis assumes that bundles are rigid helices and the cell body is an ellipsoid, and ignores hydrodynamic interactions between the bundle and cell body in estimating the torque and rotational resistance. The estimated upper bound is obtained using maximal rotational resistance and swimming velocity; therefore we expect the bound to be valid not only for our model's time-independent bundle configuration, but also for time-varying configurations of a rigid helical bundle.

The maximum estimated pitch is smaller than many of the wiggling trajectories that we observe for *B. subtilis*, indicating that factors not included in our model must be important for wiggling dynamics. These factors include static and time-dependent variations from a helical bundle geometry, non-ellipsoidal and asymmetric cell-body geometries and time-varying bundle configurations which lead to large hydrodynamic interactions with the cell body. In what follows, we investigate yet another possibility that can produce larger pitches even for rigid, helical flagella with fixed orientation and position: whereas one bundle generates too much torque, a suitable arrangement of two flagellar bundles may be able to reduce the total torque exerted by the flagella. This scenario is inspired by recent experimental observations, based on flagellar staining, which revealed that *B. subtilis* can swim using two flagellar bundles (Li 2010). Although two flagellar bundles will have twice the torque due to rotation about
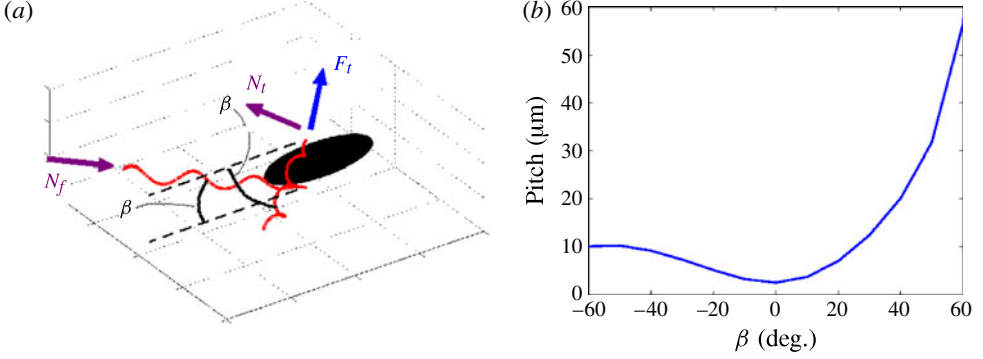
FIGURE 10. (Colour online) (*a*) Bacterium with one flagellar bundle at $\alpha_1 = 45°$, $\gamma_1 = 0°$ and $\beta_1 = \beta$, and the other bundle at $\alpha_2 = 45°$, $\gamma_2 = 0°$ and $\beta_2 = -\beta$. The flagellar thrust force from the first bundle (F_t) produces a torque (N_t) that tends to cancel the torque due to rotation of the second bundle (N_f), and vice versa. The reduced total torque can lead to a considerably larger wiggling pitch, compared to the case of a single flagellum. (*b*) The pitch P as a function of β for the geometries in panel (*a*).

their axes, the flagellar thrust is exerted along different lines of action, reducing the net torque, as illustrated in figure 10(*a*). Thus, multiple flagellar bundles can allow *B. subtilis* to generate the experimentally observed wiggling trajectories with pitch greater than 4 µm.

5. Wiggling trajectories produced by two flagellar bundles

With two flagellar bundles, the number of possible flagellar configurations rises dramatically, so we are not able to perform an exhaustive parametric study of configuration geometries. Furthermore, literature results on the precise arrangement of the two bundles are insufficient to provide guidance in this respect. However, by choosing a class of configurations, we are able to verify the physical mechanism generating large pitches described above. Consider *B. subtilis* swimming with two flagellar bundles, both with the same helical geometry as used in our model of one flagellar bundle. The first bundle is attached with angles $\alpha_1 = 45°$ and $\gamma_1 = 0°$, with the orientation angle $\beta_1 = \beta$ allowed to vary. The second bundle is attached on the opposite side, with angles $\alpha_2 = -45°$ and $\gamma_2 = 0°$ and $\beta_2 = -\beta_1 = -\beta$ (figure 10*a*).

Based on the mechanism proposed above, we expect that, if β is positive, then the line of action of the flagellar thrust due to the first bundle creates a torque that tends to cancel the torque due to the rotation of the second bundle, and vice versa (figure 10*a*). As the angle β increases from zero, more torque is cancelled and hence larger pitches are expected. On the other hand, for negative values of β, the torque due to thrust enhances the torque due to rotation of the other bundle, and so the pitch should remain small.

We use our BEM to calculate the wiggling trajectories of the configurations with two flagellar bundles shown in figure 10(*a*). In these calculations, each bundle is discretized using 12-gon cross-sections, but the cross-sections are slightly more separated than in the single bundle, so that the total number of stokeslets used in each bundle is 3304. The cell body is still discretized with 1712 stokeslets. In figure 10(*b*), we plot the pitch of the wiggling trajectory as a function of β. In accordance with our expectation, the pitch remains small when β is negative and increases for positive

Trajectory	α_1 (deg.)	α_2 (deg.)	β_1 (deg.)	β_2 (deg.)	γ_1 (deg.)	γ_2 (deg.)	Calculated pitch (μm)	Calculated radius (μm)
1	35	−35	23	−22.5	21	0	7.9	1.6
2	18	0	20	−0	0	0	3.0	0.6
3	55	−55	47	−47	5.1	0	10.3	0.4

TABLE 1. Examples of calculated wiggling trajectories produced by two flagellar bundles with pitch and radius similar to numbered trajectories in figure 1. The angles α_1, β_1 and γ_1 are for the first bundle, while α_2, β_2 and γ_2 are for the second bundle.

values of β. This corroborates our explanation of the wiggling kinematics produced by two flagellar bundles.

Multiple-bundle configurations can lead to the trajectories with pitch larger than 4 μm that we observed for *B. subtilis*, but which could not be generated by a single bundle in our BEM calculations. Because the configurations shown in figure 10(*a*) are symmetric upon rotation around the major axis of the cell body by 180°, for these configurations Ω and V must both be parallel to the major axis, and thus the wiggling trajectory radius is zero. However, by introducing small asymmetries into this flagellar configuration, V and Ω become slightly misaligned and wiggling trajectory radii similar to those observed in our imaging experiments can be generated while maintaining longer pitches. Consider the three wiggling trajectories labelled in figure 1(*c*). Using our BEM, we find bacterial geometries involving two flagellar bundles that result in trajectories which closely approximate these three trajectories, and present them in table 1. Given the number of degrees of freedom, we do not expect there to be a unique configuration generating any particular wiggling trajectory. However, these results show that our physical understanding of the kinematics of swimming with two bundles allows us to find configurations producing three realistic wiggling trajectories, suggesting that many *B. subtilis* may swim using more than one bundle at a time.

6. Discussion

A bacterial trajectory is made of smoothly varying runs and rather abrupt tumbles. It has long been known that, even during runs, the trajectory is not straight because of rotational Brownian diffusion. We have shown that, in addition to this effect, the trajectory is not straight due to flagella pushing the body off-axis, which results in helical wiggling trajectories. We expect that wiggling trajectories are the norm among bacteria, because perfect on-axis pushing by the flagellum is unlikely. Since peritrichous bacteria may form flagellar bundles at many possible positions, and with many orientations relative to the cell body, their trajectories will have a wide distribution of wiggling amplitudes.

We imaged the trajectories of *B. subtilis* bacteria and found that the average pitch and radius of the wiggling trajectories are 8.9 ± 6.0 μm and 0.91 ± 0.81 μm, respectively, with a wide distribution of pitches and radii. We used a BEM based on the method of regularized stokeslets (Cortez 2001) to calculate the wiggling swimming trajectories of *B. subtilis* for the entire range of possible time-independent flagellar bundle configurations. For a single rigid flagellum, our model produced no wiggling pitch greater than 4 μm. Using physical estimates based on torque-balance

considerations, we showed that pitch is limited for bacteria swimming with a single bundle by the relatively large torque exerted by the bundle. We then showed that model geometries of *B. subtilis* swimming with two flagellar bundles can generate the wiggling trajectories observed in our experiments with pitch greater than 4 μm.

B. subtilis swimming with multiple flagellar bundles have recently been observed using flagellar staining and videomicroscopy (Li 2010). The bundles can be aligned off-axis, tangentially to the cell surface. Little is known about the dynamics of swimming with multiple bundles. Our approach of combining experimental tracking of wiggling trajectories with quantitative modelling provides an additional, complementary method of interrogating this type of propulsion.

Based on the combined errors associated with modelling the ellipsoid (§ 3.3.1), our BEM (§ 3.3.2) and our choice of mesh size (§ 3.4), we estimate that our results for pitch and radius have an error of approximately 10 %. When making detailed comparisons with observations, three additional factors must be considered.

First, we have assumed an ellipsoidal cell body 4 μm long by 1 μm wide, which matches the average size of *B. subtilis* observed in our experiments. In reality, however, there is variation in cell-body sizes and aspect ratios within a population, including asymmetric body shapes.

Second, the shape of *B. subtilis* cell bodies is not perfectly ellipsoidal, but somewhat 'pill-shaped'. We have used our BEM to model cell-body shapes consisting of a cylindrical mid-section with hemispherical caps at their ends, and found that for cell bodies with aspect ratio 4, the wiggling trajectory pitch and radius are 20 and 30 % larger, respectively, than those obtained for ellipsoidal cell bodies.

Third, we assumed that the bundle filament radius is 45 nm. We performed BEM calculations to investigate the dependence of our results on the bundle filament radius. Changing the bundle filament radius for the flagellar configuration specified by $\alpha = 30°$, $\beta = 51°$ and $\gamma = 24°$ did not affect the swimming speed V much ($V = 15.64$ μm s^{-1} for filament radius 25 nm; $V = 15.62$ μm s^{-1} for filament radius 60 nm), but the rotation rate Ω varied approximately linearly with filament radius, increasing by 51 % as the bundle filament radius increases from 25 nm ($\Omega = 34.6$ rad s^{-1}) to 60 nm ($\Omega = 52.3$ rad s^{-1}). The wiggling trajectory pitch and radius also varied approximately linearly with filament radius, decreasing by 35 % as the bundle filament radius increases from 25 nm ($P = 2.77$ μm, $R = 2.77$ μm) to 60 nm ($P = 1.79$ μm, $R = 1.86$ μm).

Combining all these errors, we estimate that, in the worst case, the maximum pitch generated by a single flagellar bundle might be approximately 10 μm. Importantly, the conclusion drawn from our model that many of the large pitches observed in wiggling trajectories of *B. subtilis* are produced by swimming with multiple bundles rather than a single bundle is robust to errors of these magnitudes, since 32 % of our observed trajectories still have pitch greater than 10 μm.

Future investigations of wiggling trajectories may incorporate additional effects not present in our minimal model for wiggling. As mentioned in § 3.2, owing to the flexibility of the hook, the orientation of flagella relative to the cell body can vary in time. This intriguing elastohydrodynamic problem could potentially impact the wiggling dynamics presented here, but will require a full treatment of fluid–structure interactions. We note that, for peritrichous bacteria, many flagella in a flagellar bundle are oriented in the same direction; hence, altering the bundle orientation requires deforming many hooks, not just one. Thus elastic deformation of flagellar bundles may be less important for peritrichous bacteria such as *B. subtilis* than elastic deformation of a single flagellum for monotrichous bacteria. Additionally, the detailed geometry of

the cell body, especially if it is curved and asymmetric, can lead to helical trajectories even for polar flagella or flagellar bundles. Finally, the bundle is a composite object consisting of many flagella, and future modelling may take into account the dynamics and detailed geometry of the flagellar bundle, which may deviate significantly from a rigid helix, especially at its base.

To date, not much attention has been paid to off-axis flagella and flagellar bundles in models of swimming bacteria. Understanding the microhydrodynamics of motile microorganisms provides fundamental information to predict the ecological implications of these organisms (Durham, Kessler & Stocker 2009). Here we have shown that a minimal model incorporating small deviations from the simplest and most widely used morphological configuration – a flagellar bundle pushing on-axis – leads to the existence of wiggling in bacterial trajectories, observed for *B. subtilis* and for a wide range of other bacterial species.

The detailed kinematics produced by the non-symmetric geometries of off-axis flagellar configurations are important for bacterial behaviours beyond the wiggling trajectories studied here. One example is the recently discovered hybrid movement pattern of certain marine bacteria (Stocker 2011; Xie *et al.* 2011), which alternate reversals with flicks of their flagellum, the flick resulting in a marked reorientation (mean of 90°). During a flick the flagellum develops a kink at the base and so is not aligned with the symmetry axis of the cell body. Therefore we expect that refining commonly used models of bacterial propulsion to incorporate off-axis flagella may shed light on a range of bacterial processes.

Acknowledgements

REFERENCES

BEARON, R. N. & PEDLEY, T. J. 2000 Modelling run-and-tumble chemotaxis in a shear flow. *Bull. Math. Biol.* **62**, 775–791.

BERG, H. C. & BROWN, D. A. 1972 Chemotaxis in *Escherichia coli* analysed by three-dimensional tracking. *Nature* **239**, 500–504.

CORTEZ, R. 2001 The method of regularized Stokeslets. *SIAM J. Sci. Comput.* **23**, 1204–1225.

CORTEZ, R., FAUCI, L. & MEDOVIKOV, A. 2005 The method of regularized Stokeslets in three dimensions: analysis, validation, and application to helical swimming. *Phys. Fluids* **17**, 031504.

CRENSHAW, H. C. 1996 A new look at locomotion in microorganisms: rotating and translating. *Am. Zool.* **36**, 608–618.

CRENSHAW, H. C., CIAMPAGLIO, C. N. & MCHENRY, N. 2000 Analysis of the three-dimensional trajectories of organisms: estimates of velocity, curvature and torsion from positional information. *J. Expl Biol.* **203**, 961–982.

DARNTON, N., TURNER, L., ROJEVSKY, S. & BERG, H. C. 2007 On torque and tumbling in swimming *Escherichia coli*. *J. Bacteriol.* **189**, 1756–1764.

DURHAM, W. M., KESSLER, J. O. & STOCKER, R. 2009 Disruption of vertical motility by shear triggers formation of thin phytoplankton layers. *Science* **323**, 1067–1070.

FLORES, H., LOBATON, E., MÉNDEZ-DIEZ, S., TLUPOVA, S. & CORTEZ, R. 2005 A study of bacterial flagellar bundling. *Bull. Math. Biol.* **67**, 137–168.

FUJII, M., SHIBATA, S. & AIZAWA, S.-I. 2008 Polar, peritrichous, and lateral flagella belong to three distinguishable flagellar families. *J. Mol. Biol.* **379**, 273–283.

GOTO, T., MASUDA, S., TERADA, K. & TAKANO, Y. 1910 Comparison between observation and boundary element analysis of bacterium swimming motion. *JSME Intl J.* C **44**, 958–963.

HAPPEL, J. & BRENNER, H. 1965 *Low Reynolds Number Hydrodynamics*. Prentice-Hall.

HIGDON, J. L. L. 1979 A hydrodynamic analysis of flagellar propulsion. *J. Fluid Mech.* **90**, 685–711.

JANSSEN, P. J. A. & GRAHAM, M. D. 2011 Coexistence of tight and loose bundled states in a model of bacterial flagellar dynamics. *Phys. Rev.* E **84**, 011910.

KELLER, J. B. & RUBINOW, S. I. 1976 Swimming of flagellated microorganisms. *Biophys. J.* **16**, 151.

LI, M. 2010 Experimental study of swimming flagellated bacteria and their collective behaviour in concentrated suspensions. PhD thesis, University of Edinburgh.

LOCSEI, J. T. & PEDLEY, T. J. 2009 Run and tumble chemotaxis in a shear flow: the effect of temporal comparisons, persistence, rotational diffusion, and cell shape. *Bull. Math. Biol.* **71**, 1089–1116.

MAGARIYAMA, Y., ICHIBA, M., NAKATA, K., BABA, K., OHTANI, T. & KUDO, S. 2005 Difference in bacterial motion between forward and backward swimming caused by the wall effect. *Biophys. J.* **88**, 3648–3658.

PERSSON, P. 2005 Mesh generation for implicit geometries. PhD thesis, Massachusetts Institute of Technology.

PHAN-THIEN, N., TRAN-CONG, T. & RAMIA, M. 1987 A boundary-element analysis of flagellar propulsion. *J. Fluid Mech.* **184**, 533–549.

PURCELL, E. M. 1977 Life at low Reynolds number. *Am. J. Phys.* **45**, 3–11.

RAMIA, M., TULLOCK, D. L. & PHAN-THIEN, N. 1993 The role of hydrodynamic interaction in the locomotion of microorganisms. *Biophys. J.* **65**, 755–778.

SHAPERE, A. & WILCZEK, F. 1989 Geometry of self-propulsion at low Reynolds number. *J. Fluid Mech.* **198**, 557.

SHUM, H., GAFFNEY, E. A. & SMITH, D. J. 2010 Modelling bacterial behaviour close to a no-slip plane boundary: the influence of bacterial geometry. *J. Fluid Mech.* **466**, 1725–1748.

SMITH, D. J., GAFFNEY, E. A., GADELHA, H., KAPUR, N. & KIRKMAN-BROWN, J. C. 2009 Bend propagation in the flagella of migrating human sperm, and its modulation by viscosity. *Cell Motil. Cytoskel.* **66**, 220–236.

STEINBERGER, B. N., PETERSEN, N., PETERMANN, H. & WEISS, D. G. 1994 Movement of magnetic bacteria in time-varying magnetic fields. *J. Fluid Mech.* **273**, 189–211.

STOCKER, R. 2011 Reverse and flick: hybrid locomotion in bacteria. *Proc. Natl Acad. Sci. USA* **108**, 2635–2636.

SZURMANT, H., MUFF, T. & ORDAL, G. W. 2004 *Bacillus subtilis* CheC and FliY are members of a novel class of CheY-P-hydrolyzing proteins in the chemotactic signal transduction cascade. *J. Biol. Chem.* **279**, 21787–21792.

TAKANO, Y., YOSHIDA, K., KUDO, S., NISHITOBA, M. & MAGARIYAMA, Y. 2003 Analysis of small deformation of helical flagellum of swimming *Vibrio alginolyticus*. *JSME Intl J.* C **46**, 1241–1247.

XIE, L., ALTINDAL, T., CHATTOPADHYAY, S. & WU, X.-L. 2011 Bacterial flagellum as a propeller and as a rudder for efficient chemotaxis. *Proc. Natl Acad. Sci.* **108**, 2246–2251.

ZIMMER, M. A., SZURMANT, H., SAULMON, M. M., COLLINS, M. A., BANT, J. S. & ORDAL, G. W. 2002 The role of heterologous receptors in mcpb-mediated signalling in *Bacillus subtilis* chemotaxis. *Mol. Microbiol.* **45**, 555–568.